

# RUN: Reversible Unfolding Network for Concealed Object Segmentation

Chunming He<sup>1</sup>, Rihan Zhang<sup>1</sup>, Fengyang Xiao<sup>1</sup>, Chenyu Fang<sup>2</sup>, Longxiang Tang<sup>2</sup>,  
Yulun Zhang<sup>3</sup>, Linghe Kong<sup>3</sup>, Deng-Ping Fan<sup>4</sup>, Kai Li<sup>5</sup>, Sina Farsiu<sup>1</sup>

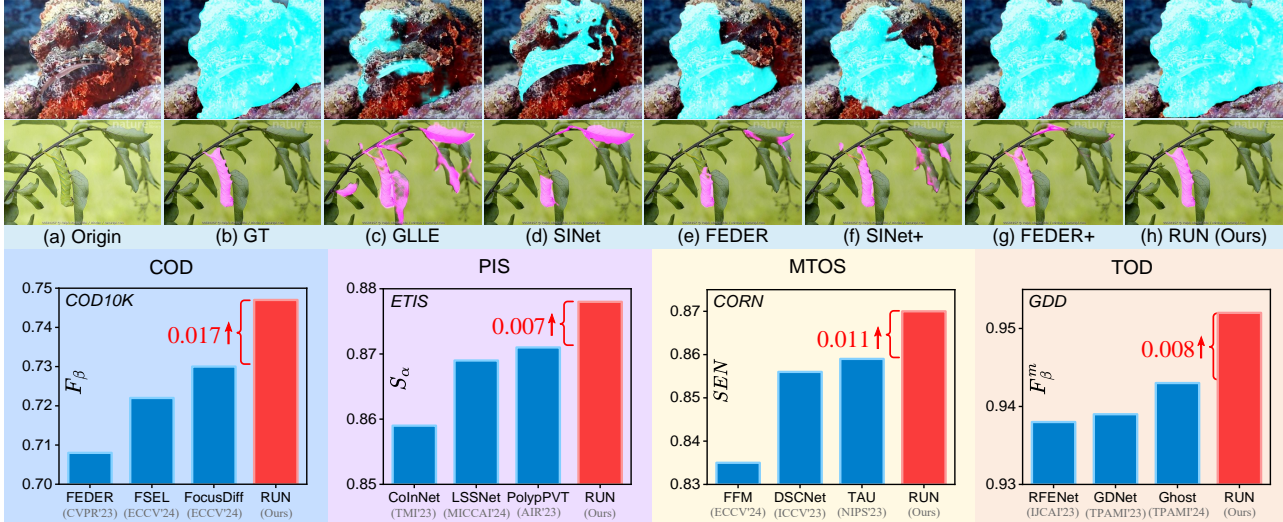


Figure 1. Results of existing COS methods. Our RUN demonstrates superiority in accurately segmenting concealed objects (in the top section) and achieves leading places across multiple COS tasks (in the bottom section): camouflaged object detection (COD), polyp image segmentation (PIS), medical tubular object segmentation (MTOS), and transparent object detection (TOD). In the top section, concealed object masks are highlighted in blue and pink, overlaid on the original images for visual clarity. FEDER+ and SINet+ indicate integrating FEDER and SINet with our RUN framework. For the bottom section, we employ commonly used datasets, methods, and metrics.

## Abstract

Existing concealed object segmentation (COS) methods frequently utilize reversible strategies to address uncertain regions. However, these approaches are typically restricted to the mask domain, leaving the potential of the RGB domain underexplored. To address this, we propose the Reversible Unfolding Network (RUN), which applies reversible strategies across both mask and RGB domains through a theoretically grounded framework, enabling accurate segmentation. RUN first formulates a novel COS model by incorporating an extra residual sparsity constraint to minimize segmentation uncertainties. The iterative optimization steps of the proposed

model are then unfolded into a multistage network, with each step corresponding to a stage. Each stage of RUN consists of two reversible modules: the Segmentation-Oriented Foreground Separation (SOFS) module and the Reconstruction-Oriented Background Extraction (ROBE) module. SOFS applies the reversible strategy at the mask level and introduces Reversible State Space to capture non-local information. ROBE extends this to the RGB domain, employing a reconstruction network to address conflicting foreground and background regions identified as distortion-prone areas, which arise from their separate estimation by independent modules. As the stages progress, RUN gradually facilitates reversible modeling of foreground and background in both the mask and RGB domains, directing the network’s attention to uncertain regions and mitigating false-positive and false-negative results. Extensive experiments demonstrate the superior performance of RUN and highlight the potential of unfolding-based frameworks for COS and other high-level vision tasks. We will release the code and models.

<sup>1</sup>BME, Duke University, Durham, NC, US. <sup>2</sup>SIGS, Tsinghua University, Shenzhen, Guangdong, China. <sup>3</sup>MoE Key Lab of Artificial Intelligence, AI Institute, Shanghai Jiao Tong University, Shanghai, China. <sup>4</sup>Nankai Institute of Advanced Research (SHENZHEN-FUTIAN), Guangdong, China. <sup>5</sup>Meta, CA, US.. Correspondence to: Sina Farsiu <sina.farsiu@duke.edu>.

## 1. Introduction

Concealed object segmentation (COS) aims to segment objects that are visually blended with their surroundings. It serves as an umbrella term with various applications, including camouflaged object detection (He et al., 2024b), polyp image segmentation (He et al., 2024a), and transparent object detection (Xiao et al., 2023), among others.

COS is a challenging problem due to the intrinsic similarity between the object and its background. Traditional methods address this challenge by relying on manually designed models with hand-crafted feature extractors tailored to subtle differences in textures, intensities, and colors (Wang et al., 2019). While offering clear interpretability, they often struggle in complex scenarios. Deep learning advances COS by leveraging its strong generalization capabilities, driven by powerful feature extraction mechanisms. Early learning-based approaches, such as SINet (Fan et al., 2020a), primarily focus on foreground regions for segmentation, often overlooking discriminative cues in the background, leading to suboptimal performance (see Fig. 1). Recent algorithms, such as FEDER (He et al., 2023b), have sought to refine segmentation masks by reversibly modeling both foreground and background regions at the mask-level.

Reversible modeling enhances the network’s capacity to extract subtle discriminative cues by directing attention to uncertain regions—pixels with values that are neither 1 nor 0—thus improving segmentation results. However, current methods restrict the application of reversible strategies to the mask level, leaving the potential of the RGB domain underexplored. Such information can assist in identifying discriminative cues and enhancing segmentation quality. As shown in Fig. 2 (d) and (e), when reversibly separating the image into foreground and background regions based on the mask, the uncertainty regions in the mask tend to manifest as color distortion in the RGB space. Addressing these translates to a more precise separation of the foreground and background. In this case, two seemingly independent tasks—object segmentation and distortion restoration—share the same optimization goal. Existing research has shown that jointly optimizing such tasks helps guide the network toward an optimal solution (Xu et al., 2023).

To achieve this, we first introduce a deep unfolding network termed the Reversible Unfolding Network (RUN) for COS. RUN established a theoretical foundation to reversibly integrate the two aforementioned tasks, rather than directly combining them, to achieve more accurate segmentation. The COS task is formulated as a foreground-background separation process, and a new segmentation model is developed by incorporating a residual sparsity constraint to reduce segmentation uncertainties. The iterative optimization steps of the model-based solution are then unfolded into a multi-stage network, with each step corresponding to a stage. Each

stage comprises two reversible modules: the Segmentation-Oriented Foreground Separation (SOFS) module and the Reconstruction-Oriented Background Extraction (ROBE) module. By integrating optimization solutions with deep networks, our RUN framework achieves an effective balance between interpretability and generalizability.

We implement the reversible strategy within the mask domain in SOFS and within the RGB domain in ROBE. In SOFS, the mask is initially updated strictly according to the optimization solution. Subsequently, the Reversible State Space (RSS) module, recognized for its strong capacity to extract non-local information, is employed to refine the segmentation mask using the previously estimated mask and background. In ROBE, the process begins with a mathematical update of the background. A lightweight network is then used to reconstruct the entire image, while simultaneously refining the background, based on the estimated foreground and background. Since the estimation of foreground and background regions is performed by distinct modules, their assessments of concealed content can differ (see Fig. 2 (d) and (f)). Regions of conflicting judgments are identified as distortion-prone areas during the reconstruction process (see Fig. 2 (g) and (h)). This auxiliary reconstruction task, which targets the resolution of such distortions, effectively directs the network’s attention to challenging regions where distinguishing between foreground and background is particularly difficult, improving segmentation performance.

As the stages progress, RUN incrementally facilitates reversible modeling of foreground and background in both the mask and RGB domains. This approach effectively focuses the network on uncertain regions, reducing false-positive and false-negative outcomes. Notably, RUN exhibits high flexibility, allowing seamless integration with existing methods to achieve further performance enhancements.

Our contributions are summarized as follows:

- (1) We propose RUN for the COS task. To the best of our knowledge, this represents the first application of a deep unfolding network to address the COS problem, thereby balancing interpretability and generalizability.
- (2) RUN proposes a novel COS model designed to reduce segmentation uncertainties and introduces SOFS and ROBE modules to integrate model-based optimization solutions with deep networks. By enabling reversible modeling of foreground and background across both the mask and RGB domains, RUN directs the network’s focus to uncertain regions, reducing false-positive and false-negative outcomes.
- (3) Experiments on five COS tasks, as well as salient object detection, validate the superiority of our RUN method. Besides, its plug-and-play structure underscores the effectiveness and adaptability of unfolding-based frameworks for the COS task and other high-level vision tasks.

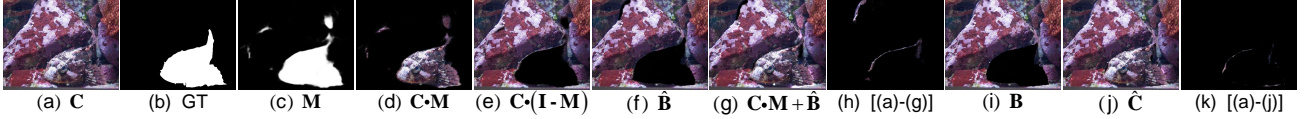


Figure 2. Correspondence between uncertainties in the mask domain and distortions in the RGB domain.  $\mathbf{C}$  is the concealed image and  $\hat{\mathbf{B}}$  is the estimated background, which has conflicting judgments of concealed regions with the mask  $\mathbf{M}$ . This conflict leads to distortion-prone areas in their direct combination (g). Panel (h) illustrates the difference between (g) and the original image (a). However, after refinement through the network  $\mathcal{B}(\cdot)$ , the reconstructed image  $\hat{\mathbf{C}}$  becomes much closer to the original image, accompanied by a refined background  $\mathbf{B}$  with improved accuracy. This refined background is passed to the next stage to further facilitate segmentation.

## 2. Related Works

**Concealed object segmentation.** Deep learning methods have advanced COS (Xiao et al., 2024). Among them, those using reversible techniques to segment from foreground and background aspects are gaining attention. PraNet (Fan et al., 2020b) introduced a parallel structure with reversible attention to enhance segmentation. FEDER (He et al., 2023b) used foreground and background masks to identify concealed objects with edge assistance. BiRefNet (Zheng et al., 2024) proposed a reconstruction module to refine the mask with gradient information. However, they only focus on the mask level, leaving the RGB domain underexplored. Hence, we propose the first deep unfolding network, RUN, for COS. RUN proposes a novel COS model and introduces SOFS and ROBE. By integrating optimization solutions with deep networks, RUN enables reversible modeling across mask and RGB domains, improving segmentation accuracy.

**Deep unfolding network.** The deep unfolding network, a well-established technique in low-level vision, integrates model-based and learning-based approaches (He et al., 2023a; Fang et al., 2025), offering enhanced interpretability compared to pure learning-based methods. However, its application in high-level vision remains underexplored, primarily due to the lack of explicit intrinsic models for high-level vision tasks. In this paper, we introduce a deep unfolding network, RUN, in COS and formulate a novel COS model. RUN achieves more accurate segmentation results by integrating optimization-based solutions with deep networks, verifying its potential for advancing COS.

## 3. Methodology

### 3.1. COS Model

A concealed image  $\mathbf{C}$  can be decomposed into its foreground region  $\mathbf{F}$  and background region  $\mathbf{B}$ , expressed as

$$\mathbf{C} = \mathbf{F} + \mathbf{B}. \quad (1)$$

Based on Eq. (1), the foreground and background regions can be obtained by optimizing the objective function:

$$L(\mathbf{F}, \mathbf{B}) = \frac{1}{2} \|\mathbf{C} - \mathbf{F} - \mathbf{B}\|_2^2 + \beta \varphi(\mathbf{F}) + \lambda \phi(\mathbf{B}), \quad (2)$$

where  $\|\cdot\|_2$  is a  $\ell_2$ -norm for smooth.  $\varphi(\mathbf{F})$  and  $\phi(\mathbf{B})$  are regularization terms for  $\mathbf{F}$  and  $\mathbf{B}$  with two trade-off parameters  $\beta$  and  $\lambda$ . To suit the segmentation task, we directly focus

on the mask  $\mathbf{M}$ , where  $\mathbf{F} = \mathbf{C} \cdot \mathbf{M}$ , and  $\cdot$  is dot product. Substituting into Eq. (2), the objective function becomes

$$L(\mathbf{M}, \mathbf{B}) = \frac{1}{2} \|\mathbf{C} - \mathbf{C} \cdot \mathbf{M} - \mathbf{B}\|_2^2 + \mu \psi(\mathbf{M}) + \lambda \phi(\mathbf{B}), \quad (3)$$

where  $\psi(\mathbf{M})$  and  $\mu$  are the regularization term and trade-off parameter for  $\mathbf{M}$ . Due to the intrinsic ambiguity of foreground objects in concealed images and the diverse nature of their backgrounds, manually defining regularization terms for  $\mathbf{M}$  and  $\mathbf{B}$  can be challenging. To address this, we utilize deep neural networks to implicitly learn these constraints in a data-driven manner. Beyond the two intrinsic regularization terms above, we introduce an extra residual sparsity constraint  $\mathcal{S}(\cdot)$  to further refine segmentation and minimize uncertainties. This leads to the final objective function:

$$L(\mathbf{M}, \mathbf{B}) = \frac{1}{2} \|\mathbf{C} - \mathbf{C} \cdot \mathbf{M} - \mathbf{B}\|_2^2 + \mu \psi(\mathbf{M}) + \lambda \phi(\mathbf{B}) + \alpha \mathcal{S}(\mathbf{w} \cdot (\mathbf{M} - \tilde{\mathbf{M}})), \quad (4)$$

where  $\alpha$  controls the weight of the sparsity constraint,  $\mathcal{S}(\cdot)$  represents an  $\ell_1$ -norm,  $\tilde{\mathbf{M}}$  is the refined mask after uncertainty-removal mapping, and  $\mathbf{w}$  is the attention map. For a pixel located at  $(i, j)$ ,  $\tilde{\mathbf{M}}$  and  $\mathbf{w}$  can be defined as

$$\tilde{\mathbf{M}}_{(i,j)} = \begin{cases} 0.1 & \mathbf{M}_i \in [0.1, 0.4], \\ 0.9 & \mathbf{M}_i \in (0.6, 0.9], \\ \mathbf{M}_i & \text{Otherwise.} \end{cases} \quad (5)$$

$$\mathbf{w}_{(i,j)} = \begin{cases} 0 & \mathbf{M}_i \in [0.4, 0.6], \\ 1 & \text{Otherwise.} \end{cases}$$

This design encourages the generation of segmentation masks with high certainty. Following the practice of (He et al., 2024a), pixels with values in the ambiguous range  $[0.4, 0.6]$  are excluded from further consideration, while extreme values for  $\tilde{\mathbf{M}}$  are set to 0.1 and 0.9 instead of 0 and 1 to allow greater flexibility for optimization.

### 3.2. RUN

#### 3.2.1. MODEL OPTIMIZATION

We utilize the proximal gradient algorithm (Fang et al., 2025) to optimize Eq. (4), ultimately deriving the optimal mask  $\mathbf{M}^*$  and background  $\mathbf{B}^*$ :

$$\{\mathbf{M}^*, \mathbf{B}^*\} = \arg \min_{\mathbf{M}, \mathbf{B}} L(\mathbf{M}, \mathbf{B}). \quad (6)$$

The optimization process involves alternating updates of the two variables over iterations. Here we take the  $k^{\text{th}}$  stage ( $1 \leq k \leq K$ ) to present the alternative solution process.

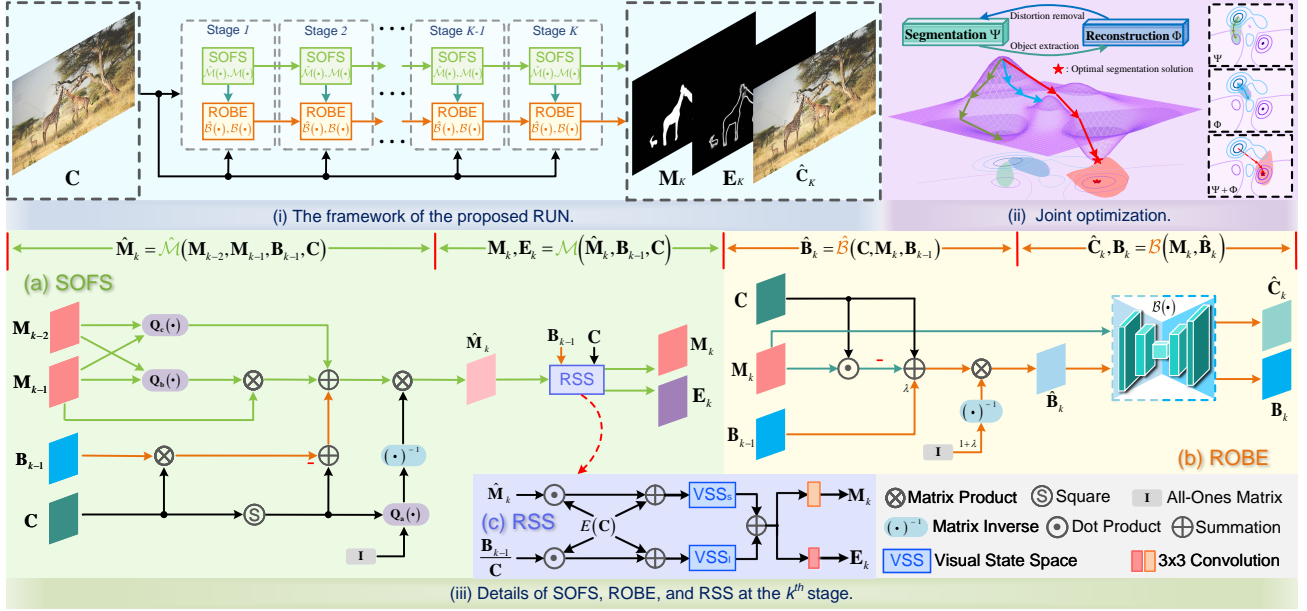


Figure 3. Framework of our RUN. The network connections in  $\hat{\mathcal{M}}(\cdot)$  and  $\hat{\mathcal{B}}(\cdot)$  are derived strictly based on mathematical principles, thus enhancing interpretability. For clarity, we replace certain redundant details with  $\mathbf{Q}_a$ ,  $\mathbf{Q}_b$ , and  $\mathbf{Q}_c$  and present  $\hat{\mathcal{M}}(\cdot)$  according to Eq. (18). The detailed connection can be seen in Fig. S1 in the Appendix. Panel (ii) illustrates that the joint optimization of image segmentation and reconstruction tasks facilitates the network’s progression toward an optimal solution.

**Optimizing  $\mathbf{M}_k$ .** First, the optimization function is partitioned to update the foreground mask  $\mathbf{M}_k$ :

$$\mathbf{M}_k = \arg \min_{\mathbf{M}} \frac{1}{2} \|\mathbf{C} - \mathbf{C} \cdot \mathbf{M} - \mathbf{B}_{k-1}\|_2^2 + \mu \psi(\mathbf{M}) + \alpha \mathcal{S}(\mathbf{w}_k \cdot (\mathbf{M} - \tilde{\mathbf{M}}_k)). \quad (7)$$

The solution comprises two terms: the gradient descent term and the proximal term. To address the proximal term, we introduce an auxiliary variable  $\hat{\mathbf{M}}_k$ , resulting in:

$$\mathbf{M}_k = \text{prox}_{\psi}(\mathbf{B}_{k-1}, \hat{\mathbf{M}}_k), \quad (8)$$

where  $\mathbf{B}_0$  is initialized as zero. Having gotten Eqs. (7) and (8),  $\hat{\mathbf{M}}_k$  can be solved by optimizing:

$$\hat{\mathbf{M}}_k = \frac{1}{2} \|\mathbf{C} - \mathbf{C} \cdot \hat{\mathbf{M}} - \mathbf{B}_{k-1}\|_2^2 + \frac{\mu}{2} \|\hat{\mathbf{M}} - \mathbf{M}_{k-1}\|_2^2 + \alpha \mathcal{S}(\mathbf{w}_k \cdot (\hat{\mathbf{M}} - \tilde{\mathbf{M}}_k)), \quad (9)$$

where  $\mathbf{M}_0$  is also initialized as zero. Note that  $\mathbf{w}_k$  and  $\tilde{\mathbf{M}}_k$  are constructed based on  $\mathbf{M}_{k-1}$ . For the term  $\mathcal{S}(\mathbf{w}_k \cdot (\hat{\mathbf{M}} - \tilde{\mathbf{M}}_k))$ , we employ a Taylor expansion rather than soft thresholding for flexibility in problem-solving. Following the practice of (Goldstein, 1977), we approximate  $\mathcal{S}(\mathbf{w}_k \cdot (\hat{\mathbf{M}} - \tilde{\mathbf{M}}_k))$  at the  $k-1^{\text{th}}$  iteration (for simplicity, we let  $\mathbf{R} = \mathbf{w}_k \cdot (\hat{\mathbf{M}} - \tilde{\mathbf{M}}_k)$ ), expressed as follows:

$$\mathcal{S}(\mathbf{R}) \approx \hat{\mathcal{S}}(\mathbf{R}, \mathbf{R}_{k-1}), \quad (10)$$

where

$$\hat{\mathcal{S}}(\mathbf{R}, \mathbf{R}_{k-1}) \leftarrow \frac{L_S}{2} \|\mathbf{R} - \mathbf{R}_{k-1}\|_2^2 + \frac{1}{L_S} \nabla \mathcal{S}(\mathbf{R}_{k-1}) \|\mathbf{R} - \mathbf{R}_{k-1}\|_2^2 + C_S, \quad (11)$$

where  $L_S$  is the Lipschitz constant.  $\nabla \mathcal{S}(\mathbf{R}_{k-1})$  is the Lipschitz continuous gradient function of  $\mathcal{S}(\mathbf{R}_{k-1})$  with  $C_S$ , a positive constant that can be omitted in optimization. Sub-

stituting into Eq. (9), we obtain the following equations:

$$\hat{\mathbf{M}}_k = \frac{1}{2} \|\mathbf{C} - \mathbf{C} \cdot \hat{\mathbf{M}} - \mathbf{B}_{k-1}\|_2^2 + \frac{\mu}{2} \|\hat{\mathbf{M}} - \mathbf{M}_{k-1}\|_2^2 + \frac{\alpha L_S}{2} \|\mathbf{R} - \mathbf{R}_{k-1} + \frac{1}{L_S} \nabla \mathcal{S}(\mathbf{R}_{k-1})\|_2^2. \quad (12)$$

Unlike  $\ell_1$ -norm methods, Eq. (12) can be solved directly by equating its derivative to zero. The closed-form solution is

$$\hat{\mathbf{M}}_k = (\mathbf{Q}_a)^{-1} (\mathbf{Q}_b \mathbf{M}_{k-1} + \mathbf{C}^2 - \mathbf{C} \mathbf{B}_{k-1} + \mathbf{Q}_c), \quad (13)$$

where  $\mathbf{Q}_a = \mathbf{C}^2 + L_S \mathbf{w}_k^2 + \mu \mathbf{I}$ ,  $\mathbf{I}$  is an all-ones matrix,  $\mathbf{Q}_b = \alpha L_S \mathbf{w}_k \mathbf{w}_{k-1} + \mu \mathbf{I}$ ,  $\mathbf{Q}_c = \alpha L_S \mathbf{w}_k (\mathbf{w}_k \cdot \tilde{\mathbf{M}}_k - \mathbf{Q}_d) - \alpha \mathbf{w}_k \nabla \mathcal{S}(\mathbf{w}_{k-1} \cdot \mathbf{M}_{k-1} - \mathbf{Q}_d)$ , and  $\mathbf{Q}_d = \mathbf{w}_{k-1} \cdot \tilde{\mathbf{M}}_{k-1}$ .

**Optimizing  $\mathbf{B}_k$ .** The optimization function of  $\mathbf{B}_k$  is

$$\mathbf{B}_k = \arg \min_{\mathbf{B}} \frac{1}{2} \|\mathbf{C} - \mathbf{C} \cdot \mathbf{M}_k - \mathbf{B}\|_2^2 + \lambda \phi(\mathbf{B}). \quad (14)$$

Same as the optimization rule for  $\mathbf{M}_k$ , the gradient descent term and the proximal term are correspondingly defined as:

$$\hat{\mathbf{B}}_k = \frac{1}{2} \|\mathbf{C} - \mathbf{C} \cdot \mathbf{M}_k - \hat{\mathbf{B}}\|_2^2 + \frac{\lambda}{2} \|\hat{\mathbf{B}} - \mathbf{B}_{k-1}\|_2^2, \quad (15)$$

$$\mathbf{B}_k = \text{prox}_{\phi}(\hat{\mathbf{B}}_k, \mathbf{M}_k). \quad (16)$$

The closed-form solution of  $\hat{\mathbf{B}}_k$  can be acquired similarly:

$$\hat{\mathbf{B}}_k = ((1 + \lambda) \mathbf{I})^{-1} (\lambda \mathbf{B}_{k-1} + \mathbf{C} - \mathbf{C} \cdot \mathbf{M}_k). \quad (17)$$

### 3.2.2. DEEP UNFOLDING MECHANISM

We unfold the iterative optimization steps of the model-based solution into a multi-stage network, termed Reversible Unfolding Network (RUN), with each step corresponding to a stage. As shown in Fig. 3, each stage has two reversible modules: the Segmentation-Oriented Foreground Separation

tion (SOFS) and Reconstruction-Oriented Background Extraction (ROBE) modules.

**SOFS.** SOFS, derived from Eqs. (8) and (13), utilizes  $\hat{\mathcal{M}}(\cdot)$  and  $\mathcal{M}(\cdot)$  to compute the optimization solution  $\hat{\mathbf{M}}$  and the refined mask  $\mathbf{M}$  at each stage, respectively. Given  $\mathbf{B}_{k-1}$ ,  $\mathbf{M}_{k-1}$ , and  $\mathbf{M}_{k-2}$ , we define  $\hat{\mathbf{M}}_k$  as follows:

$$\begin{aligned} \hat{\mathbf{M}}_k &= \hat{\mathcal{M}}(\mathbf{B}_{k-1}, \mathbf{M}_{k-1}, \mathbf{M}_{k-2}, \mathbf{C}), \\ &= (\mathbf{Q}_a)^{-1}(\mathbf{Q}_b \mathbf{M}_{k-1} + \mathbf{C}^2 - \mathbf{C} \mathbf{B}_{k-1} + \mathbf{Q}_c). \end{aligned} \quad (18)$$

Eq. (18) retains the same formulation as Eq. (13), but all originally fixed parameters, including  $\nabla S(\cdot)$ , are relaxed to be learnable, improving the model’s generalizability.

To refine the initial mask  $\hat{\mathbf{M}}_k$ , we introduce the Reversible State Space (RSS) module  $RSS(\cdot)$ , which has a robust capacity for non-local information extraction. The RSS module incorporates two Visual State Space (VSS)  $VSS(\cdot)$  modules (Liu et al., 2024b) with distinct perception fields. The VSS with a small perception field locally refines uncertain regions along the edges from the foreground perspective, while the VSS with a large perception field globally identifies missed segmented regions from the background perspective. This dual-perception mechanism ensures both accurate and comprehensive segmentation results. Following (He et al., 2023b), we also integrate an auxiliary edge output  $\mathbf{E}_k$  to further enhance segmentation performance. Consequently, the computation of  $\mathbf{M}_k$  and  $\mathbf{E}_k$  is defined as:

$$\begin{aligned} \mathbf{M}_k, \mathbf{E}_k &= \mathcal{M}(\mathbf{B}_{k-1}, \hat{\mathbf{M}}_k, \mathbf{C}) = RSS(\mathbf{B}_{k-1}, \hat{\mathbf{M}}_k, \mathbf{C}), \\ &= conv3(VSS_s(E(\mathbf{C}) \cdot \hat{\mathbf{M}}_k + E(\mathbf{C}))) \\ &\quad + VSS_l(E(\mathbf{C}) \cdot (\mathbf{B}_{k-1}/\mathbf{C}) + E(\mathbf{C})), \end{aligned} \quad (19)$$

where  $conv3$  is  $3 \times 3$  convolution.  $VSS_s(\cdot)$  and  $VSS_l(\cdot)$  have small and large perception fields, incorporating convolutions with varying kernel sizes. For brevity, we omit the detailed description of VSS. Unlike low-level vision tasks, segmentation tasks, particularly inherently complex COS, strongly depend on semantic information. It is challenging to extract this fully using a shallow network. To address this, we adopt the common practice of leveraging deep features  $E(\mathbf{C})$ , extracted from an encoder (default: ResNet50 (He et al., 2016)). Rather than directly processing the concealed image, this approach enables the extraction of subtle discriminative features, achieving accurate segmentation.

**ROBE.** In ROBE, the calculation of  $\hat{\mathbf{B}}_k$  relies on  $\hat{\mathcal{B}}(\cdot)$ , similar to Eq. (15) but with the fixed parameters made learnable:

$$\begin{aligned} \hat{\mathbf{B}}_k &= \hat{\mathcal{B}}(\mathbf{B}_{k-1}, \mathbf{M}_k, \mathbf{C}), \\ &= ((1 + \lambda) \mathbf{I})^{-1}(\lambda \mathbf{B}_{k-1} + \mathbf{C} - \mathbf{C} \cdot \mathbf{M}_k). \end{aligned} \quad (20)$$

This is essentially a dynamic fusion of the previously estimated background and the reversed foreground derived in the current stage. To refine  $\hat{\mathbf{B}}_k$ , we propose a simple U-shaped network (Xu et al., 2023) with three layers, denoted as  $\mathcal{B}(\cdot)$ . However, as shown in Fig. 2, since separate modules estimate the foreground and background, their interpreta-

tions of the concealed content may differ. Hence, regions with conflicting interpretations are identified as distortion-prone areas in reconstruction. To address this, the network also generates a reconstructed result  $\hat{\mathbf{C}}_k$ , formulated as:

$$\mathbf{B}_k, \hat{\mathbf{C}}_k = \mathcal{B}(\hat{\mathbf{B}}_k, \mathbf{M}_k). \quad (21)$$

$\hat{\mathbf{C}}_k$  is designed to be consistent with the concealed image, thereby mitigating distortions. This alignment fosters consistent judgments between SOFS and ROBE for foreground-background separation, improving segmentation accuracy. As the stages progress, RUN incrementally facilitates reversible modeling of the foreground and background in both the mask and RGB domains. This iterative process directs the network’s attention to regions of uncertainty, reducing false-positive and false-negative outcomes. Hence, RUN ensures robust and accurate segmentation performance.

**Loss function.** The loss function comprises a segmentation term and a reconstruction term. We adopt the training strategy from FEDER (He et al., 2023b) for the segmentation part. A mean square error loss governs the reconstruction component. The overall loss function is defined as

$$\begin{aligned} L_t &= \sum_{k=1}^K \frac{1}{2^{K-k}} [L_{BCE}^w(\mathbf{M}_k, GT_s) + L_{IoU}^w(\mathbf{M}_k, GT_s)] \\ &\quad + L_{dice}(\mathbf{E}_k, GT_e) + \|\hat{\mathbf{C}}_k - \mathbf{C}\|_2^2, \end{aligned} \quad (22)$$

where  $K$  is the number of stages.  $L_{BCE}^w$  is the weighted binary cross-entropy loss,  $L_{IoU}^w$  is the weighted intersection-over-union loss, and  $L_{dice}$  is the dice loss.  $GT_s$  and  $GT_e$  are the ground truth of the segmentation mask and edge.

## 4. Experiments

**Implementation details.** We implement our method using PyTorch on two RTX4090 GPUs. In line with (Fan et al., 2020a), we incorporate deep features from encoder-shaped networks into our framework. All images are resized to  $352 \times 352$  for the training and testing phases. During training, we use the Adam optimizer with momentum parameters (0.9, 0.999). The batch size is set to 36, and the initial learning rate is configured to 0.0001, which is reduced by 0.1 every 80 epochs. The stage number  $K$  is set as 4. Additional parameters inherited from traditional methods are optimized in a learnable manner with random initialization.

### 4.1. Comparative Evaluation

We conduct experiments on various COS tasks and compare our performance with SOTA methods using standard metrics. Details on datasets and metrics are in Appendix A.1. Our superiority in concealed defect detection and salient object detection is verified in Appendices A.2 and A.3. For fairness, all results are evaluated with consistent task-specific evaluation tools. Except for COD, other tasks have few pub-

Table 1. Results on camouflaged object detection. SegMaR-1/-4 are SegMaR with one or four stages. The best results are marked in **bold**. For the ResNet50 backbone in the common setting, the best two results are in **red** and **blue** fonts.

| Methods   | Backbones | CHAMELEON      |                    |                   |                     | CAMO           |                    |                   |                     | COD10K         |                    |                   |                     | NC4K           |                    |                   |                     |
|---|-----------|----------------|--------------------|-------------------|---------------------|----------------|--------------------|-------------------|---------------------|----------------|--------------------|-------------------|---------------------|----------------|--------------------|-------------------|---------------------|
|   |           | $M \downarrow$ | $F_\beta \uparrow$ | $E_\phi \uparrow$ | $S_\alpha \uparrow$ | $M \downarrow$ | $F_\beta \uparrow$ | $E_\phi \uparrow$ | $S_\alpha \uparrow$ | $M \downarrow$ | $F_\beta \uparrow$ | $E_\phi \uparrow$ | $S_\alpha \uparrow$ | $M \downarrow$ | $F_\beta \uparrow$ | $E_\phi \uparrow$ | $S_\alpha \uparrow$ |
| Common Setting: Single Input Scale and Single Stage |           |                |                    |                   |                     |                |                    |                   |                     |                |                    |                   |                     |                |                    |                   |                     |
| SINet (Fan et al., 2020a)                           | ResNet50  | 0.034          | 0.823              | 0.936             | 0.872               | 0.092          | 0.712              | 0.804             | 0.745               | 0.043          | 0.667              | 0.864             | 0.776               | 0.058          | 0.768              | 0.871             | 0.808               |
| LSR (Lv et al., 2021)                               | ResNet50  | 0.030          | 0.835              | 0.935             | 0.890               | 0.080          | 0.756              | 0.838             | 0.787               | 0.037          | 0.699              | 0.880             | 0.804               | 0.048          | 0.802              | 0.890             | 0.834               |
| FEDER (He et al., 2023b)                            | ResNet50  | <b>0.028</b>   | <b>0.850</b>       | 0.944             | 0.892               | 0.070          | 0.775              | 0.870             | 0.802               | 0.032          | 0.715              | 0.892             | 0.810               | 0.046          | 0.808              | 0.900             | 0.842               |
| FGANet (Zhai et al., 2023)                          | ResNet50  | 0.030          | 0.838              | <b>0.945</b>      | 0.891               | 0.070          | 0.769              | 0.865             | 0.800               | 0.032          | 0.708              | 0.894             | 0.803               | 0.047          | 0.800              | 0.891             | 0.837               |
| FocusDiff (Zhao et al., 2024)                       | ResNet50  | <b>0.028</b>   | 0.843              | 0.938             | 0.890               | <b>0.069</b>   | 0.772              | <b>0.883</b>      | <b>0.812</b>        | <b>0.031</b>   | <b>0.730</b>       | <b>0.897</b>      | 0.820               | <b>0.044</b>   | <b>0.810</b>       | <b>0.902</b>      | <b>0.850</b>        |
| FSEL (Sun et al., 2024)                             | ResNet50  | 0.029          | 0.847              | 0.941             | <b>0.893</b>        | <b>0.069</b>   | <b>0.779</b>       | <b>0.881</b>      | <b>0.816</b>        | 0.032          | 0.722              | 0.891             | <b>0.822</b>        | 0.045          | 0.807              | 0.901             | 0.847               |
| RUN (Ours)  | ResNet50  | <b>0.027</b>   | <b>0.855</b>       | <b>0.952</b>      | <b>0.895</b>        | 0.070          | <b>0.781</b>       | 0.868             | 0.806               | <b>0.030</b>   | <b>0.747</b>       | <b>0.903</b>      | <b>0.827</b>        | <b>0.042</b>   | <b>0.824</b>       | <b>0.908</b>      | <b>0.851</b>        |
| BSA-Net (Zhu et al., 2022)                          | Res2Net50 | 0.027          | 0.851              | 0.946             | 0.895               | 0.079          | 0.768              | 0.851             | 0.796               | 0.034          | 0.723              | 0.891             | 0.818               | 0.048          | 0.805              | 0.897             | 0.841               |
| FEDER (He et al., 2023b)                            | Res2Net50 | 0.026          | 0.856              | 0.947             | 0.903               | <b>0.066</b>   | 0.807              | 0.897             | 0.836               | 0.029          | 0.748              | 0.911             | 0.844               | 0.042          | 0.824              | 0.913             | <b>0.862</b>        |
| RUN (Ours)  | Res2Net50 | <b>0.024</b>   | <b>0.879</b>       | <b>0.956</b>      | <b>0.907</b>        | <b>0.066</b>   | <b>0.815</b>       | <b>0.905</b>      | <b>0.843</b>        | <b>0.028</b>   | <b>0.764</b>       | <b>0.914</b>      | <b>0.849</b>        | <b>0.041</b>   | <b>0.830</b>       | <b>0.917</b>      | 0.859               |
| HitNet (Hu et al., 2023)                            | PVT V2    | 0.024          | 0.861              | 0.944             | 0.907               | 0.060          | 0.791              | 0.892             | 0.834               | 0.027          | 0.790              | 0.922             | 0.847               | 0.042          | 0.825              | 0.911             | 0.858               |
| CamoFocus (Khan et al., 2024)                       | PVT V2    | 0.023          | 0.869              | 0.953             | 0.906               | <b>0.044</b>   | <b>0.861</b>       | 0.924             | 0.870               | 0.022          | <b>0.818</b>       | 0.931             | 0.868               | 0.031          | 0.862              | 0.932             | 0.886               |
| RUN (Ours)  | PVT V2    | <b>0.021</b>   | <b>0.877</b>       | <b>0.958</b>      | <b>0.916</b>        | 0.045          | <b>0.861</b>       | <b>0.934</b>      | <b>0.877</b>        | <b>0.021</b>   | 0.810              | <b>0.941</b>      | <b>0.878</b>        | <b>0.030</b>   | <b>0.868</b>       | <b>0.940</b>      | <b>0.892</b>        |
| Other Setting: Multiple Input Scales (MIS)          |           |                |                    |                   |                     |                |                    |                   |                     |                |                    |                   |                     |                |                    |                   |                     |
| ZoomNet (Pang et al., 2022)                         | ResNet50  | 0.024          | 0.858              | 0.943             | 0.902               | 0.066          | 0.792              | 0.877             | 0.820               | 0.029          | 0.740              | 0.888             | 0.838               | 0.043          | 0.814              | 0.896             | 0.853               |
| FEDER (He et al., 2023b)                            | ResNet50  | 0.023          | 0.869              | 0.959             | 0.906               | <b>0.064</b>   | 0.801              | 0.893             | 0.827               | 0.028          | 0.756              | 0.913             | 0.837               | 0.041          | 0.832              | 0.915             | 0.859               |
| RUN (Ours)  | ResNet50  | <b>0.022</b>   | <b>0.878</b>       | <b>0.967</b>      | <b>0.911</b>        | <b>0.064</b>   | <b>0.807</b>       | <b>0.902</b>      | <b>0.832</b>        | <b>0.027</b>   | <b>0.772</b>       | <b>0.920</b>      | <b>0.843</b>        | <b>0.040</b>   | <b>0.836</b>       | <b>0.922</b>      | <b>0.868</b>        |
| Other Setting: Multiple Stages (MS)                 |           |                |                    |                   |                     |                |                    |                   |                     |                |                    |                   |                     |                |                    |                   |                     |
| SegMaR-4 (Jia et al., 2022)                         | ResNet50  | 0.025          | 0.855              | 0.955             | 0.906               | 0.071          | 0.779              | 0.865             | 0.815               | 0.033          | 0.737              | 0.896             | 0.833               | 0.047          | 0.793              | 0.892             | 0.845               |
| FEDER-4 (He et al., 2023b)                          | ResNet50  | 0.025          | 0.874              | 0.964             | 0.907               | 0.067          | 0.809              | 0.886             | 0.822               | 0.028          | 0.752              | 0.917             | 0.851               | 0.042          | 0.827              | 0.917             | 0.863               |
| RUN-4 (Ours)  | ResNet50  | <b>0.024</b>   | <b>0.889</b>       | <b>0.968</b>      | <b>0.913</b>        | <b>0.066</b>   | <b>0.815</b>       | <b>0.893</b>      | <b>0.829</b>        | <b>0.027</b>   | <b>0.769</b>       | <b>0.926</b>      | <b>0.857</b>        | <b>0.041</b>   | <b>0.833</b>       | <b>0.925</b>      | <b>0.870</b>        |

Table 2. Results on polyp image segmentation.

| Methods                      | CVC-ColonDB      |                 |                     | ETIS             |                 |                     |
|------------------------------|------------------|-----------------|---------------------|------------------|-----------------|---------------------|
|                              | mDice $\uparrow$ | mIoU $\uparrow$ | $S_\alpha \uparrow$ | mDice $\uparrow$ | mIoU $\uparrow$ | $S_\alpha \uparrow$ |
| PraNet (Fan et al., 2020b)   | 0.709            | 0.640           | 0.819               | 0.628            | 0.567           | 0.794               |
| CASCADE (Rahman, 2023)       | 0.809            | 0.731           | 0.867               | 0.781            | <b>0.706</b>    | 0.853               |
| PolypPVT (Dong et al., 2023) | 0.808            | 0.727           | 0.865               | <b>0.787</b>     | <b>0.706</b>    | <b>0.871</b>        |
| CoInNet (Jain et al., 2023)  | 0.797            | 0.729           | <b>0.875</b>        | 0.759            | 0.690           | 0.859               |
| LSSNet (Wang et al., 2024)   | <b>0.820</b>     | <b>0.741</b>    | 0.867               | 0.779            | 0.701           | 0.867               |
| RUN (Ours)                   | <b>0.822</b>     | <b>0.742</b>    | <b>0.880</b>        | <b>0.788</b>     | <b>0.709</b>    | <b>0.878</b>        |

Table 3. Results on medical tubular object segmentation.

| Methods                    | DRIVE            |                |                | CORN             |                |                |
|----------------------------|------------------|----------------|----------------|------------------|----------------|----------------|
|                            | mDice $\uparrow$ | AUC $\uparrow$ | SEN $\uparrow$ | mDice $\uparrow$ | AUC $\uparrow$ | SEN $\uparrow$ |
| CS2-Net (Mou et al., 2021) | 0.795            | <b>0.983</b>   | 0.822          | 0.607            | 0.960          | 0.817          |
| DSCNet (Qi et al., 2023)   | 0.805            | 0.955          | 0.830          | 0.618            | <b>0.964</b>   | 0.856          |
| SGAT (Lin et al., 2023)    | <b>0.806</b>     | 0.953          | <b>0.832</b>   | 0.639            | 0.961          | 0.853          |
| TAU (Gupta et al., 2024)   | 0.798            | 0.977          | 0.825          | 0.643            | 0.949          | <b>0.859</b>   |
| FFM (Huang et al., 2025)   | 0.791            | 0.972          | 0.830          | <b>0.647</b>     | 0.952          | 0.835          |
| RUN (Ours)                 | <b>0.812</b>     | <b>0.985</b>   | <b>0.845</b>   | <b>0.652</b>     | <b>0.962</b>   | <b>0.870</b>   |

licly open-sourced methods, limiting quantitative analysis.

**Camouflaged object detection.** As shown in Table 1, our method achieves SOTA performance across all three settings. In the common setting, it outperforms competing approaches across all three backbones: ResNet50 (He et al., 2016), Res2Net50 (Gao et al., 2019), and PVT V2 (Wang et al., 2022). This superior performance on four datasets, particularly on the largest dataset, *COD10K*, and the largest testing dataset, *NC4K*, underscores the robustness and generalization capabilities of our RUN framework. Furthermore, in the MIS and MS settings, our RUN adheres to the evaluation protocols of FEDER (He et al., 2023b) and delivers improved results over existing methods. As illustrated in Fig. 4, our method generates more complete and accurate segmentation maps. This is attributed to our jointly

Table 4. Results on transparent object detection.

| Methods                        | GDD             |                          |                | GSD             |                          |                |
|--------------------------------|-----------------|--------------------------|----------------|-----------------|--------------------------|----------------|
|                                | mIoU $\uparrow$ | $F_\beta^{max} \uparrow$ | $M \downarrow$ | mIoU $\uparrow$ | $F_\beta^{max} \uparrow$ | $M \downarrow$ |
| GDNet (Mei et al., 2020)       | 0.876           | 0.937                    | 0.063          | 0.790           | 0.869                    | 0.069          |
| EBLNet (He et al., 2021)       | 0.870           | 0.922                    | 0.064          | 0.817           | 0.878                    | 0.059          |
| RFENet (Fan et al., 2023b)     | 0.886           | 0.938                    | 0.057          | <b>0.865</b>    | <b>0.931</b>             | <b>0.048</b>   |
| IEBAF (Han et al., 2024)       | 0.887           | <b>0.944</b>             | 0.056          | 0.861           | 0.926                    | 0.049          |
| GhostingNet (Yan et al., 2024) | <b>0.893</b>    | 0.943                    | <b>0.054</b>   | 0.838           | 0.904                    | 0.055          |
| RUN (Ours)                     | <b>0.895</b>    | <b>0.952</b>             | <b>0.051</b>   | <b>0.866</b>    | <b>0.938</b>             | <b>0.043</b>   |

reversible modeling at both the mask and RGB levels.

**Medical concealed object segmentation.** We conducted experiments on two medical COS tasks, including polyp image segmentation (*CVC-ColonDB* and *ETIS* datasets) and medical tubular object segmentation (*DRIVE* and *CORN* datasets). Considering that recent SOTAs commonly use Transformer-based encoders, we adopt PVT V2 as our default encoder. As shown in Tables 2 and 3, our method achieves top performance across three tasks. Furthermore, the results in Fig. 4 confirm the effect of our approach in segmenting small polyps and fine vessels and nerves.

**Transparent object detection.** Accurately segmenting transparent objects is crucial for autonomous driving. As demonstrated in Table 4 and Fig. 4, our RUN surpasses existing methods on two datasets, providing more precise segmentation of transparent objects compared to other approaches. These results highlight our potential to contribute to the advancement of autonomous driving.

## 4.2. Ablation Study

We conduct ablation studies on *COD10K* of the COD task.

**Effect of SOFS.** As presented in Table 5, replacing the deep

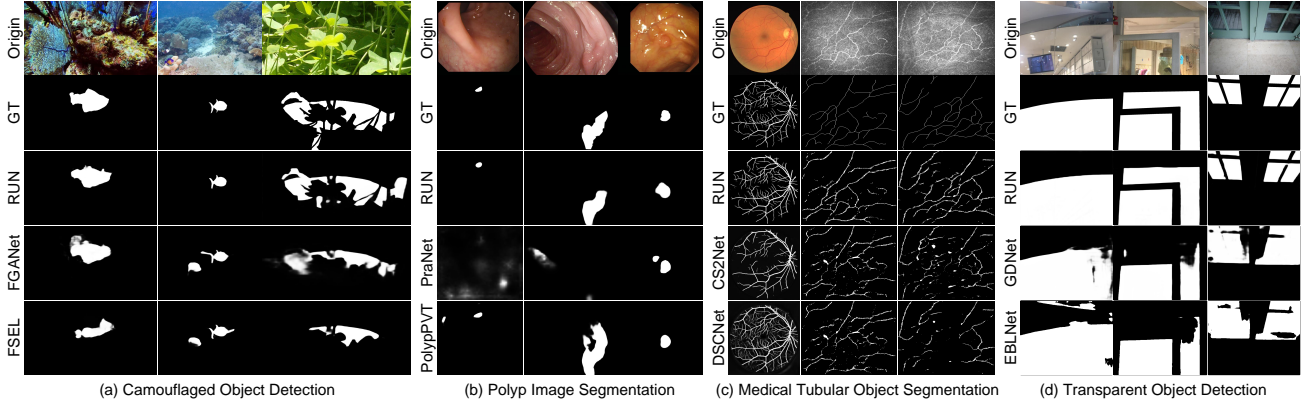


Figure 4. Visual comparison on COD, PIS, MTOS, and TOD tasks.

Table 5. Ablation study in the COD task on *COD10K*.

| Metrics             | Effect of SOFS       |         |         |                       |                              |                    | Effect of ROBE  |   |                 | Fixed →<br>Learnable | RUN<br>(Ours) |
|---------------------|----------------------|---------|---------|-----------------------|------------------------------|--------------------|---|---|-----------------|----------------------|---------------|
|                     | $C \rightarrow E(C)$ | w/o RSS | w/o VSS | w/o prior $\bar{M}_k$ | w/o prior $\mathbf{B}_{k-1}$ | w/o $\mathbf{E}_k$ | $\mathcal{B}_1(\bullet) \rightarrow \mathcal{B}(\bullet)$ | $\mathcal{B}_2(\bullet) \rightarrow \mathcal{B}(\bullet)$ | w/o $\bar{C}_k$ |                      |               |
| $M \downarrow$      | 0.053                | 0.034   | 0.031   | 0.032                 | 0.031                        | 0.031              | 0.030   | 0.030   | 0.031           | 0.032                | 0.030         |
| $F_\beta \uparrow$  | 0.617                | 0.710   | 0.740   | 0.728                 | 0.735                        | 0.733              | 0.746   | 0.749   | 0.736           | 0.731                | 0.747         |
| $E_\phi \uparrow$   | 0.825                | 0.887   | 0.897   | 0.891                 | 0.893                        | 0.890              | 0.905   | 0.906   | 0.898           | 0.896                | 0.903         |
| $S_\alpha \uparrow$ | 0.746                | 0.805   | 0.825   | 0.820                 | 0.826                        | 0.823              | 0.826   | 0.828   | 0.824           | 0.822                | 0.827         |

Table 6. Effect of our COS model. CM, PM, OS, and DL are shorts for conventional model, proposed model, optimization solution, and deep learning.

| Metrics             | PM+OS          | CM1+DL | CM2+DL | CM3+DL | CM4+DL | CM5+DL | PM+DL (Ours) | Metrics             | $K = 1$ | $K = 2$        | $K = 4$ (Ours) | $K = 6$ | $K = 8$ |
|---------------------|----------------|--------|--------|--------|--------|--------|--------------|---------------------|---------|----------------|----------------|---------|---------|
|                     | $M \downarrow$ | 0.062  | 0.032  | 0.031  | 0.031  | 0.031  | 0.032        |                     | 0.030   | $M \downarrow$ | 0.033          | 0.031   | 0.030   |
| $F_\beta \uparrow$  | 0.573          | 0.729  | 0.735  | 0.733  | 0.740  | 0.735  | 0.747        | $F_\beta \uparrow$  | 0.715   | 0.727          | 0.747          | 0.749   | 0.751   |
| $E_\phi \uparrow$   | 0.802          | 0.899  | 0.896  | 0.895  | 0.898  | 0.892  | 0.903        | $E_\phi \uparrow$   | 0.885   | 0.893          | 0.903          | 0.905   | 0.905   |
| $S_\alpha \uparrow$ | 0.733          | 0.823  | 0.824  | 0.821  | 0.823  | 0.823  | 0.827        | $S_\alpha \uparrow$ | 0.803   | 0.812          | 0.827          | 0.826   | 0.830   |

features  $E(C)$  with the concealed image results in performance decline, highlighting the critical role of incorporating deep features into the DUN-based framework. Additionally, we evaluate the impact of the state space-based structure by removing the RSS and VSS modules. The effectiveness of our reversible strategy is further validated by excluding the foreground prior  $\bar{M}_k$  and the background prior  $\mathbf{B}_{k-1}$ . Finally, we confirm the utility of integrating the auxiliary edge output, contributing to performance improvements.

**Effect of ROBE.** As shown in Table 5, when replacing  $\mathcal{B}(\bullet)$  with other large-scale networks, *i.e.*, the CNN-based network  $\mathcal{B}_1(\bullet)$  (Xu et al., 2023) and Transformer-based network  $\mathcal{B}_2(\bullet)$  (Fang et al., 2023), we observe no significant performance gains. This suggests that a simple network is sufficient for background extraction and image reconstruction. Furthermore, when the reconstructed output  $\bar{C}_k$  is removed, our RUN also produces suboptimal results.

**Other configurations in RUN.** We validate the effect of various configurations in RUN. As shown in Table 5, allowing originally fixed parameters to be learnable enhances performance. Furthermore, we compare our model with CM1 to CM5, as detailed in Table 6. CM1 corresponds to Eq. (3). CM2 also employs Eq. (4) for optimization but applies the  $\ell_1$ -norm to the first term and employs soft thresholding (He et al., 2023a) to solve  $\mathcal{S}(\bullet)$ . CM3-CM5 represent ablated

Table 7. Analysis of stage number  $K$ . We have surpassed most compared methods when  $K = 2$ .

versions of the refined mask and weighted map in Eq. (4): CM3 removes the weighted map  $w$ . CM4 modifies the refined range of pixel values from  $[0.1, 0.4] \& (0.6, 0.9]$  to  $[0.1, 0.3] \& (0.7, 0.9]$ , with corresponding adjustments to the weighted map. CM5 extends the range to include all pixel values, assigning 0.5 to the foreground region. As shown in Table 6, our approach achieves superior performance across traditional solutions and learning-based unfolding strategies. Moreover, as verified in Table 7, we analyze the optimal stage number for our method. To balance performance and computational efficiency, we set  $K = 4$ . Under this configuration, the feature maps from the last four layers of the encoder are progressively sent to the four stages, with features from deeper layers transferred first.

### 4.3. Further Analysis, Applications, and Meanings

**Performance on small objects or multiple objects.** Small objects and multiple objects are challenging for lacking discriminative cues. To evaluate our performance on the two conditions, we filtered images from *COD10K* that satisfy these criteria, resulting in 1,084 images having concealed objects smaller than a quarter of the entire image and 186 images with multiple concealed objects. As shown in Tables 8 and 9, while the performance of all methods declines, our approach consistently outperforms the competition.

Table 8. Results on small object images (1,084 images).

| Metrics             | SegMaR | FEDER | FGANet | FocusDiff | FSEL  | RUN (Ours)   |
|---------------------|--------|-------|--------|-----------|-------|--------------|
| $M \downarrow$      | 0.049  | 0.044 | 0.044  | 0.042     | 0.043 | <b>0.040</b> |
| $F_\beta \uparrow$  | 0.605  | 0.646 | 0.642  | 0.670     | 0.668 | <b>0.682</b> |
| $E_\phi \uparrow$   | 0.831  | 0.855 | 0.852  | 0.859     | 0.847 | <b>0.866</b> |
| $S_\alpha \uparrow$ | 0.765  | 0.777 | 0.776  | 0.781     | 0.776 | <b>0.789</b> |

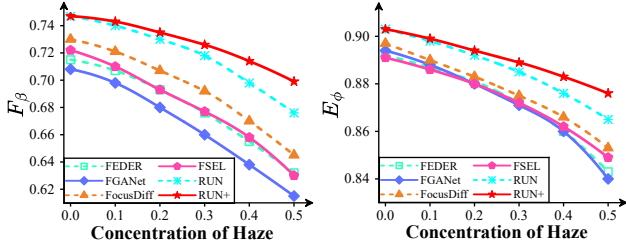


Figure 5. Performance in degraded COS scenarios.

Table 10. Potential of RUN to serve as a refiner, where ‘‘FEDER-R’’ means refining FEDER’s results with RUN.

| Metrics             | FEDER | FEDER-R | FGANet | FGANet-R | FSEL  | FSEL-R |
|---------------------|-------|---------|--------|----------|-------|--------|
| $M \downarrow$      | 0.032 | 0.031   | 0.032  | 0.032    | 0.032 | 0.031  |
| $F_\beta \uparrow$  | 0.715 | 0.721   | 0.708  | 0.716    | 0.722 | 0.725  |
| $E_\phi \uparrow$   | 0.892 | 0.897   | 0.894  | 0.897    | 0.891 | 0.890  |
| $S_\alpha \uparrow$ | 0.810 | 0.812   | 0.803  | 0.805    | 0.822 | 0.825  |

**Performance on degraded COS scenarios.** To assess the impact of environmental degradation, we followed (He et al., 2023a) to simulate haze on concealed images in *COD10K* and then evaluated the ability of the compared methods to resist degradation. As illustrated in Fig. 5, performance degrades as the haze concentration increases. However, our RUN demonstrates superior resilience to haze degradation, attributed to its multi-modality reversible modeling strategy. To enhance robustness, we replaced our reconstruction network  $\mathcal{B}(\cdot)$  with a more complex network from CoRUN (Fang et al., 2025), termed  $\mathcal{B}_3(\cdot)$ , which includes a pretrained dehazing model. This brought a novel unfolding network, RUN+, with  $\mathcal{B}_3(\cdot)$  incorporating the pretrained model. Fig. 5 indicates integrating  $\mathcal{B}_3(\cdot)$  enhances RUN’s robustness in resisting haze degradation. This underscores the potential of RUN in addressing degraded scenarios.

**Potential applications of RUN.** First, we test the effect of our RUN as a refiner, specifically by initializing  $M_0$  with the results of existing methods. As shown in Table 10, our approach can enhance the performance of SOTA methods without requiring retraining. Furthermore, we incorporate the core structures of existing methods into our RUN framework, followed by retraining the entire network. This integration yields even greater improvements, demonstrating that the unfolding framework can function as a plug-and-play solution to enhance the performance of existing methods. For example, as shown in Fig. 6, we observe that while error predictions from FEDER influence FEDER-R, FEDER+ demonstrates better resilience to such errors.

**Meanings of our framework.** Beyond introducing the deep

Table 9. Results on multi-object images (186 images).

| Metrics             | SegMaR | FEDER | FGANet | FocusDiff | FSEL  | RUN (Ours)   |
|---------------------|--------|-------|--------|-----------|-------|--------------|
| $M \downarrow$      | 0.076  | 0.068 | 0.065  | 0.062     | 0.062 | <b>0.060</b> |
| $F_\beta \uparrow$  | 0.436  | 0.480 | 0.481  | 0.500     | 0.496 | <b>0.505</b> |
| $E_\phi \uparrow$   | 0.797  | 0.813 | 0.810  | 0.818     | 0.820 | <b>0.827</b> |
| $S_\alpha \uparrow$ | 0.695  | 0.709 | 0.709  | 0.716     | 0.717 | <b>0.730</b> |

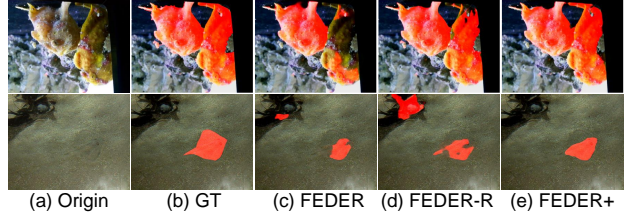


Figure 6. Potential applications of RUN. The concealed object masks are highlighted in red and overlaid on the original images.

Table 11. Generalization of RUN, where ‘‘FEDER+’’ means integrating our framework into FEDER.

| Metrics             | FEDER | FEDER+ | FGANet | FGANet+ | FSEL  | FSEL+ |
|---------------------|-------|--------|--------|---------|-------|-------|
| $M \downarrow$      | 0.032 | 0.031  | 0.032  | 0.031   | 0.032 | 0.030 |
| $F_\beta \uparrow$  | 0.715 | 0.726  | 0.708  | 0.730   | 0.722 | 0.738 |
| $E_\phi \uparrow$   | 0.892 | 0.902  | 0.894  | 0.901   | 0.891 | 0.905 |
| $S_\alpha \uparrow$ | 0.810 | 0.816  | 0.803  | 0.808   | 0.822 | 0.830 |

unfolding network to high-level vision for the first time and enabling reversible modeling across both mask and RGB domains, the proposed RUN framework offers the potential to establish a *unified vision strategy*. By combining image segmentation and image reconstruction, our RUN introduces a novel approach to unifying low-level and high-level vision. As shown in Fig. S2 in the appendix, unlike existing strategies, such as bi-level optimization (Xu et al., 2023), our unfolding-based combination strategy is underpinned by explicit theoretical guarantees with the two models better coupled. Moreover, as shown in Fig. 5 RUN+, using more complex low-level vision algorithms results in a strong ability to resist complex degradation. This motivates further exploration of unfolding-based combination strategies to enhance high-level vision algorithms’ resistance to environmental degradation and imaging interference. Simultaneously, it promotes low-level vision algorithms by integrating deep semantic information and high-level guidance. Together, these advancements ensure practical applicability in both real-world high-level and low-level vision tasks.

## 5. Conclusions

This paper proposes RUN to formulate the COS task as a foreground-background separation model. Its optimized solution is unfolded into a multistage network, where each stage comprises two reversible modules: SOFS and ROBE. SOFS applies the reversible strategy at the mask level and introduces RSS for non-local information extraction. ROBE employs a reconstruction network to address conflicting foreground and background regions in the RGB domain. Extensive experiments verify the superiority of RUN.



## References

- Deng, X., Zhang, P., Liu, W., and Lu, H. Recurrent multi-scale transformer for high-resolution salient object detection. In *ACM MM*, pp. 7413–7423, 2023. 13
- Dong, B., Wang, W., Fan, D.-P., Li, J., Fu, H., and Shao, L. Polyp-pvt: Polyp segmentation with pyramid vision transformers. *CAAI Artif. Intell. Res.*, 2, 2023. 6
- Everingham, M., Van Gool, L., Williams, C. K., Winn, J., and Zisserman, A. The pascal visual object classes (voc) challenge. *Int. J. Comput. Vis.*, 88:303–338, 2010. 13
- Fan, D.-P., Cheng, M.-M., Liu, Y., and Li, T. Structure-measure: A new way to evaluate foreground maps. In *ICCV*, pp. 4548–4557, 2017. 12
- Fan, D.-P., Ji, G.-P., Sun, G., Cheng, M.-M., and Shen, J. Camouflaged object detection. In *CVPR*, pp. 2777–2787, 2020a. 2, 5, 6, 12
- Fan, D.-P., Ji, G.-P., and Zhou, T. Prantet: Parallel reverse attention network for polyp segmentation. In *MICCAI*, pp. 263–273, 2020b. 3, 6
- Fan, D.-P., Ji, G.-P., Cheng, M.-M., and Shao, L. Concealed object detection. *IEEE Trans. Pattern Anal. Mach. Intell.*, 2021a. 12, 13
- Fan, D.-P., Ji, G.-P., Qin, X., and Cheng, M.-M. Cognitive vision inspired object segmentation metric and loss function. *Scientia Sinica Informationis*, 6(6), 2021b. 12
- Fan, D.-P., Ji, G.-P., Xu, P., Cheng, M.-M., Sakaridis, C., and Van Gool, L. Advances in deep concealed scene understanding. *Visual Intell.*, 1(1):16, 2023a. 12
- Fan, K., Wang, C., Wang, Y., Wang, C., Yi, R., and Ma, L. Rfenet: towards reciprocal feature evolution for glass segmentation. In *IJCAI*, pp. 717–725, 2023b. 6
- Fang, C., Zhang, Y., Ye, T., Li, K., Tang, L., Guo, Z., Li, X., and Farsiu, S. Reti-diff: Illumination degradation image restoration with retinex-based latent diffusion model. *arXiv preprint arXiv:2311.11638*, 2023. 7
- Fang, C., He, C., Xiao, F., Zhang, Y., Tang, L., Zhang, Y., Li, K., and Li, X. Real-world image dehazing with coherence-based label generator and cooperative unfolding network. *NeurIPS*, 2025. 3, 8
- Gao, S.-H., Cheng, M.-M., Zhao, K., Zhang, X.-Y., Yang, M.-H., and Torr, P. Res2net: A new multi-scale backbone architecture. *IEEE Trans. Pattern Anal. Mach. Intell.*, 43(2):652–662, 2019. 6
- Goldstein, A. A. Optimization of lipschitz continuous functions. *Math. Program.*, 13:14–22, 1977. 4
- Gupta, S., Zhang, Y., Hu, X., Prasanna, P., and Chen, C. Topology-aware uncertainty for image segmentation. *NeurIPS*, 36, 2024. 6
- Han, D., Lee, S., Zhang, C., Yoon, H., Kwon, H., Kim, H.-C., and Choo, H.-G. Internal-external boundary attention fusion for glass surface segmentation. *arXiv preprint arXiv:2307.00212*, 2024. 6
- He, C., Li, K., and Zhang, Y. Degradation-resistant unfolding network for heterogeneous image fusion. In *ICCV*, pp. 611–621, 2023a. 3, 7, 8
- He, C., Li, K., Zhang, Y., Tang, L., and Zhang, Y. Camouflaged object detection with feature decomposition and edge reconstruction. In *CVPR*, pp. 22046–22055, 2023b. 2, 3, 5, 6
- He, C., Li, K., Zhang, Y., Xu, G., and Tang, L. Weakly-supervised concealed object segmentation with sam-based pseudo labeling and multi-scale feature grouping. *NeurIPS*, 2024a. 2, 3
- He, C., Li, K., Zhang, Y., Zhang, Y., Guo, Z., and Li, X. Strategic preys make acute predators: Enhancing camouflaged object detectors by generating camouflaged objects. *ICLR*, 2024b. 2
- He, H., Li, X., Cheng, G., Shi, J., Tong, Y., Meng, G., Prinnet, V., and Weng, L. Enhanced boundary learning for glass-like object segmentation. In *ICCV*, pp. 15859–15868, 2021. 6
- He, K., Zhang, X., Ren, S., and Sun, J. Deep residual learning for image recognition. In *CVPR*, pp. 770–778, 2016. 5, 6
- Hu, X., Wang, S., Qin, X., Dai, H., Ren, W., Luo, D., Tai, Y., and Shao, L. High-resolution iterative feedback network for camouflaged object detection. In *AAAI*, volume 37, pp. 881–889, 2023. 6, 13
- Huang, J., Zhou, Y., Luo, Y., Liu, G., Guo, H., and Yang, G. Representing topological self-similarity using fractal feature maps for accurate segmentation of tubular structures. In *ECCV*, pp. 143–160. Springer, 2025. 6
- Jain, S., Atale, R., Gupta, A., Mishra, U., Seal, A., Ojha, A., Jaworek-Korjakowska, J., and Krejcar, O. Coinnet: A convolution-involution network with a novel statistical attention for automatic polyp segmentation. *IEEE Trans. Med. Imaging*, 42(12):3987–4000, 2023. 6
- Jia, Q., Yao, S., and Liu, Y. Segment, magnify and reiterate: Detect camouflaged objects hard way. In *CVPR*, pp. 713–722, 2022. 6

- Khan, A., Khan, M., Gueaieb, W., El Saddik, A., De Masi, G., and Karray, F. Camofocus: Enhancing camouflage object detection with split-feature focal modulation and context refinement. In *WACV*, pp. 1434–1443, 2024. 6
- Le, T.-N., Nguyen, T. V., Nie, Z., Tran, M.-T., and Sugimoto, A. Anabranh network for camouflaged object segmentation. *Comput. Vis. Image Underst.*, 184:45–56, 2019. 12
- Li, G. and Yu, Y. Visual saliency based on multiscale deep features. In *CVPR*, pp. 5455–5463, 2015. 13
- Li, Y., Hou, X., Koch, C., Rehg, J. M., and Yuille, A. L. The secrets of salient object segmentation. In *CVPR*, pp. 280–287, 2014. 13
- Lin, J. and He, Z. Rich context aggregation with reflection prior for glass surface detection. In *CVPR*, pp. 13415–13424, 2021. 12
- Lin, J., Huang, X., Zhou, H., Wang, Y., and Zhang, Q. Stimulus-guided adaptive transformer network for retinal blood vessel segmentation in fundus images. *Med. Image Anal.*, 89:102929, 2023. 6
- Liu, N., Zhang, N., Wan, K., Shao, L., and Han, J. Visual saliency transformer. In *ICCV*, pp. 4722–4732, 2021. 13
- Liu, N., Luo, Z., Zhang, N., and Han, J. Vst++: Efficient and stronger visual saliency transformer. *IEEE Trans. Pattern Anal. Mach. Intell.*, 2024a. 13
- Liu, Y., Tian, Y., Zhao, Y., Yu, H., Xie, L., Wang, Y., Ye, Q., and Liu, Y. Vmamba: Visual state space model. In *NeurIPS*, 2024b. 5
- Lv, Y., Zhang, J., Dai, Y., Li, A., Liu, B., Barnes, N., and Fan, D.-P. Simultaneously localize, segment and rank the camouflaged objects. In *CVPR*, pp. 11591–11601, 2021. 6, 12
- Ma, Y., Liu, J., Liu, Y., Fu, H., Hu, Y., Cheng, J., Qi, H., Wu, Y., Zhang, J., and Zhao, Y. Structure and illumination constrained gan for medical image enhancement. *IEEE Trans. Med. Imaging*, 40(12):3955–3967, 2021. 12
- Margolin, R., Zelnik-Manor, L., and Tal, A. How to evaluate foreground maps? In *CVPR*, pp. 248–255, 2014. 12
- Mei, H., Yang, X., Wang, Y., Liu, Y., and He, S. Don’t hit me! glass detection in real-world scenes. In *CVPR*, pp. 3687–3696, 2020. 6, 12
- Mei, H., Yang, X., Yu, L., Zhang, Q., Wei, X., and Lau, R. W. Large-field contextual feature learning for glass detection. *IEEE Trans. Pattern Anal. Mach. Intell.*, 2023. 12
- Mou, L., Zhao, Y., Fu, H., Liu, Y., Cheng, J., Zheng, Y., Su, P., Yang, J., Chen, L., Frangi, A. F., et al. Cs2-net: Deep learning segmentation of curvilinear structures in medical imaging. *Med. Image Anal.*, 67:101874, 2021. 6
- Pang, Y., Zhao, X., Xiang, T.-Z., Zhang, L., and Lu, H. Zoom in and out: A mixed-scale triplet network for camouflaged object detection. In *CVPR*, pp. 2160–2170, 2022. 6
- Qi, Y., He, Y., Qi, X., Zhang, Y., and Yang, G. Dynamic snake convolution based on topological geometric constraints for tubular structure segmentation. In *ICCV*, pp. 6070–6079, 2023. 6, 12
- Rahman, M. M. Medical image segmentation via cascaded attention decoding. In *WACV*, pp. 6222–6231, 2023. 6
- Silva, J., Histace, A., Romain, O., and Dray, X. Toward embedded detection of polyps in wce images for early diagnosis. *Int. J. Comput. Assist. Radiol. Surg.*, 9:283–293, 2014. 12
- Skurowski, P., Abdulameer, H., and Błaszczczyk, J. Animal camouflage analysis: Chameleon database. *Unpublished manuscript*, pp. 7, 2018. 12
- Sun, Y., Xu, C., Yang, J., Xuan, H., and Luo, L. Frequency-spatial entanglement learning for camouflaged object detection. In *ECCV*, pp. 343–360, 2024. 6
- Tajbakhsh, N., Gurudu, S. R., and Liang, J. Automated polyp detection in colonoscopy videos using shape and context information. *IEEE Trans. Med. Imaging*, 35(2): 630–644, 2015. 12
- Wang, L., Lu, H., and Wang, Y. Learning to detect salient objects with image-level supervision. In *CVPR*, pp. 136–145, 2017. 13
- Wang, W., Xie, E., Li, X., Fan, D.-P., Song, K., Liang, D., Lu, T., Luo, P., and Shao, L. Pvt v2: Improved baselines with pyramid vision transformer. *Comput. Vis. Media*, 8(3):415–424, 2022. 6
- Wang, W., Sun, H., and Wang, X. Lssnet: A method for colon polyp segmentation based on local feature supplementation and shallow feature supplementation. In *MICCAI*, pp. 446–456. Springer, 2024. 6, 12
- Wang, X., Deng, L., and Xu, G. Image threshold segmentation based on gile histogram. In *CPSCOM*, pp. 410–415. IEEE, 2019. 2
- Wang, Y., Wang, R., Fan, X., Wang, T., and He, X. Pixels, regions, and objects: Multiple enhancement for salient object detection. In *CVPR*, pp. 10031–10040, 2023. 13

- Xiao, F., Zhang, P., and He, C. Concealed object segmentation with hierarchical coherence modeling. In *CAAI ICAI*, pp. 16–27, 2023. 2
- Xiao, F., Hu, S., Shen, Y., and He, C. A survey of camouflaged object detection and beyond. *arXiv preprint arXiv:2408.14562*, 2024. 3
- Xie, C., Xia, C., Ma, M., Zhao, Z., Chen, X., and Li, J. Pyramid grafting network for one-stage high resolution saliency detection. In *CVPR*, pp. 11717–11726, 2022. 13
- Xu, G., Yan, J., Tang, L., and Zhang, Y. Hqg-net: Unpaired medical image enhancement with high-quality guidance. *IEEE Trans. Neural Networks Learn. Syst.*, 2023. 2, 5, 7, 8
- Yan, Q., Xu, L., Shi, J., and Jia, J. Hierarchical saliency detection. In *CVPR*, pp. 1155–1162, 2013. 13
- Yan, T., Gao, J., Xu, K., Zhu, X., Huang, H., Li, H., Wah, B., and Lau, R. W. Ghostingnet: A novel approach for glass surface detection with ghosting cues. *IEEE Trans. Pattern Anal. Mach. Intell.*, 2024. 6
- Yang, C., Zhang, L., Lu, H., Ruan, X., and Yang, M.-H. Saliency detection via graph-based manifold ranking. In *CVPR*, pp. 3166–3173, 2013. 13
- Yang, X., Zhu, H., Mao, G., and Xing, S. Oaformer: Occlusion aware transformer for camouflaged object detection. In *ICME*, pp. 1421–1426. IEEE, 2023. 13
- Yi, Y., Zhang, N., Zhou, W., Shi, Y., Xie, G., and Wang, J. Gponet: A two-stream gated progressive optimization network for salient object detection. *Pattern Recogn.*, 150:110330, 2024. 13
- Yin, B., Zhang, X., Fan, D.-P., Jiao, S., Cheng, M.-M., Van Gool, L., and Hou, Q. Camoformer: Masked separable attention for camouflaged object detection. *IEEE Trans. Pattern Anal. Mach. Intell.*, 2024. 13
- Zhai, W., Cao, Y., and Zhang, J. Exploring figure-ground assignment mechanism in perceptual organization. In *NeurIPS*, volume 35, 2023. 6
- Zhao, J., Li, X., Yang, F., Zhai, Q., Luo, A., Jiao, Z., and Cheng, H. Focusdiffuser: Perceiving local disparities for camouflaged object detection. In *ECCV*, pp. 181–198, 2024. 6
- Zheng, P., Gao, D., Fan, D.-P., Liu, L., Laaksonen, J., Ouyang, W., and Sebe, N. Bilateral reference for high-resolution dichotomous image segmentation. *CAAI AIR*, 2024. 3, 14
- Zhu, H., Li, P., Xie, H., Yan, X., Liang, D., Chen, D., Wei, M., and Qin, J. I can find you! boundary-guided separated attention network for camouflaged object detection. In *AAAI*, volume 36, pp. 3608–3616, 2022. 6
- Zhuge, M., Fan, D.-P., Liu, N., Zhang, D., Xu, D., and Shao, L. Salient object detection via integrity learning. *IEEE Trans. Pattern Anal. Mach. Intell.*, 2022. 13

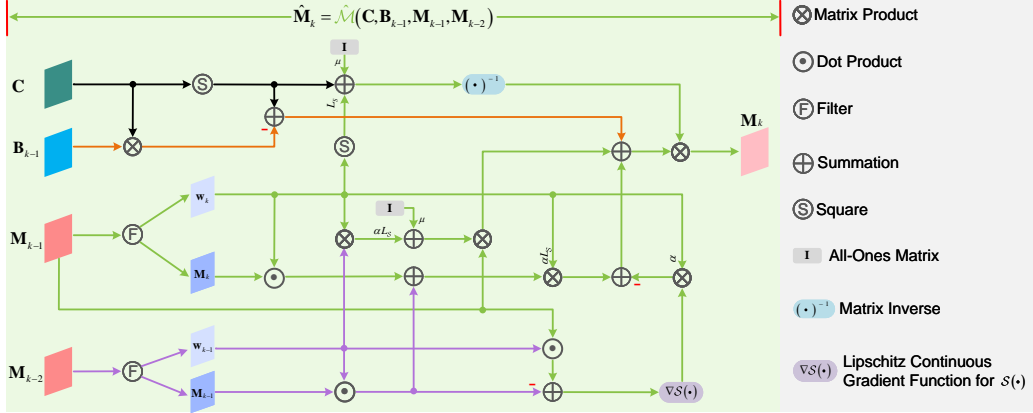


Figure S1. Details of  $\hat{M}(\cdot)$ , where the connections in  $\hat{M}(\cdot)$  are derived strictly based on mathematical principles, thus enhancing interpretability.

## A. Experiment

### A.1. Datasets and metrics

**Camouflaged object detection.** In this task, we follow the standard practice of SINet (Fan et al., 2020a) and perform experiments on four datasets: *CHAMELEON* (Skurowski et al., 2018), *CAMO* (Le et al., 2019), *COD10K* (Fan et al., 2021a), and *NC4K* (Lv et al., 2021). The *CHAMELEON* dataset comprises 76 images, while the *CAMO* dataset contains 1,250 images divided into 8 classes. The *COD10K* dataset includes 5,066 images categorized into 10 super-classes, and *NC4K* serves as the largest test set, with 4,121 images. For training, we use 1,000 images from *CAMO* and 3,040 images from *COD10K*. The remaining images from these two datasets, along with all images from the other datasets, constitute the test set. To evaluate performance, we employ four widely-used metrics: mean absolute error ( $M$ ), adaptive F-measure ( $F_\beta$ ) (Margolin et al., 2014), mean E-measure ( $E_\phi$ ) (Fan et al., 2021b), and structure measure ( $S_\alpha$ ) (Fan et al., 2017). Superior performance is indicated by lower values of  $M$  and higher values of  $F_\beta$ ,  $E_\phi$ , and  $S_\alpha$ .

**Medical concealed object segmentation.** We evaluate the performance of our method on two specific tasks: polyp image segmentation and medical tubular object segmentation. For polyp image segmentation, we utilize two benchmarks: *CVC-ColonDB* (Tajbakhsh et al., 2015) and *ETIS* (Silva et al., 2014). The training protocol follows the setup of LSSNet (Wang et al., 2024). Quantitative evaluation is conducted using three commonly adopted metrics: mean Dice (mDice), mean Intersection over Union (mIoU), and structure measure ( $S_\alpha$ ), where higher values indicate better performance. For medical tubular object segmentation, we evaluate our method on the *DRIVE*<sup>1</sup> and *CORN* (Ma et al., 2021) datasets, with training and inference conducted separately for each dataset. For the *DRIVE* dataset, training and inference adhere to the dataset’s predefined splits. For the *CORN* dataset, the last 70% of the data is used for training, while the first 30% serves as the test set. Following DSCNet (Qi et al., 2023), we employ three evaluation metrics: mDice, area under the ROC curve (AUC), and sensitivity (SEN), with higher values reflecting better performance. To ensure a fair comparison with state-of-the-art medical concealed object segmentation methods, which predominantly utilize transformer-based encoders, we adopt PVT V2 as the backbone for our encoder.

**Transparent object detection.** For a fair comparison, we use PVT V2 as our default backbone and conduct experiments on two datasets: *GDD* (Mei et al., 2020) and *GSD* (Lin & He, 2021). The training set consists of 2,980 images from *GDD* and 3,202 images from *GSD*, while the remaining images are reserved for inference. Consistent with GNet-B (Mei et al., 2023), we evaluate performance using several metrics, including mIoU, and maximum F-measure ( $F_\beta^{max}$ ). Superior performance is indicated by lower values for  $M$ , or higher values for mIoU and  $F_\beta^{max}$ .

**Concealed defect detection.** In this task, we utilize PVT V2 as the default backbone. Consistent with established practices, we evaluate the generalization capacity of our RUN framework on the concealed defect detection task. Specifically, we use the model trained on the COD task to segment concealed objects in the *CDS2K* dataset (Fan et al., 2023a). Eight evaluation metrics are employed, where higher values indicate better performance for all metrics except MAE, for which lower values are preferred.

<sup>1</sup><http://www.isi.uu.nl/Research/Databases/DRIVE/>

Table S1. Restuls on concealed defect detection.

| Methods                        | $S_\alpha \uparrow$ | $M \downarrow$ | $E_\phi^{ad} \uparrow$ | $E_\phi \uparrow$ | $E_\phi^{max} \uparrow$ | $F_\beta \uparrow$ | $F_\beta^{mean} \uparrow$ | $F_\beta^{max} \uparrow$ |
|--------------------------------|---------------------|----------------|------------------------|-------------------|-------------------------|--------------------|---------------------------|--------------------------|
| SINet V2 (Fan et al., 2021a)   | 0.551               | 0.102          | 0.509                  | 0.567             | <b>0.597</b>            | 0.223              | 0.248                     | 0.258                    |
| HitNet (Hu et al., 2023)       | 0.563               | 0.118          | 0.574                  | 0.564             | 0.570                   | <b>0.298</b>       | 0.298                     | 0.299                    |
| CamoFormer (Yin et al., 2024)  | <b>0.589</b>        | <b>0.100</b>   | <b>0.590</b>           | <b>0.588</b>      | 0.596                   | <b>0.330</b>       | <b>0.329</b>              | <b>0.339</b>             |
| OAFoFormer (Yang et al., 2023) | 0.541               | 0.121          | 0.479                  | 0.535             | 0.591                   | 0.216              | 0.239                     | 0.252                    |
| RUN (Ours)                     | <b>0.590</b>        | <b>0.068</b>   | <b>0.601</b>           | <b>0.595</b>      | <b>0.611</b>            | <b>0.298</b>       | <b>0.299</b>              | <b>0.303</b>             |

Table S2. Restuls on salient object detection.

| Methods                      | <i>DUT-OMRON</i> |                    |                   |                     | <i>DUTS-test</i> |                    |                   |                     | <i>ECSSD</i>   |                    |                   |                     | <i>HKU-IS</i>  |                    |                   |                     | <i>PASCAL-S</i> |                    |                   |                     |
|------------------------------|------------------|--------------------|-------------------|---------------------|------------------|--------------------|-------------------|---------------------|----------------|--------------------|-------------------|---------------------|----------------|--------------------|-------------------|---------------------|-----------------|--------------------|-------------------|---------------------|
|                              | $M \downarrow$   | $F_\beta \uparrow$ | $E_\phi \uparrow$ | $S_\alpha \uparrow$ | $M \downarrow$   | $F_\beta \uparrow$ | $E_\phi \uparrow$ | $S_\alpha \uparrow$ | $M \downarrow$ | $F_\beta \uparrow$ | $E_\phi \uparrow$ | $S_\alpha \uparrow$ | $M \downarrow$ | $F_\beta \uparrow$ | $E_\phi \uparrow$ | $S_\alpha \uparrow$ | $M \downarrow$  | $F_\beta \uparrow$ | $E_\phi \uparrow$ | $S_\alpha \uparrow$ |
| VST (Liu et al., 2021)       | 0.058            | 0.755              | 0.871             | 0.850               | 0.037            | 0.828              | 0.919             | 0.896               | 0.033          | 0.910              | 0.951             | 0.932               | 0.029          | 0.897              | 0.952             | 0.928               | 0.061           | 0.816              | 0.902             | 0.872               |
| ICON-P (Zhuge et al., 2022)  | 0.047            | <b>0.793</b>       | <b>0.896</b>      | <b>0.865</b>        | <b>0.022</b>     | <b>0.882</b>       | <b>0.950</b>      | <b>0.917</b>        | <b>0.024</b>   | <b>0.933</b>       | 0.964             | 0.940               | <b>0.022</b>   | <b>0.925</b>       | 0.967             | <b>0.935</b>        | <b>0.051</b>    | <b>0.847</b>       | <b>0.921</b>      | <b>0.882</b>        |
| PGNet (Xie et al., 2022)     | <b>0.045</b>     | 0.767              | 0.887             | 0.855               | 0.027            | 0.851              | 0.922             | 0.911               | <b>0.024</b>   | 0.920              | 0.955             | 0.932               | 0.024          | 0.912              | 0.958             | 0.934               | 0.052           | 0.838              | 0.912             | 0.875               |
| MENet (Wang et al., 2023)    | <b>0.045</b>     | 0.782              | 0.891             | 0.849               | 0.028            | 0.860              | 0.937             | 0.905               | 0.033          | 0.906              | 0.954             | 0.928               | 0.023          | 0.910              | 0.966             | 0.927               | 0.054           | 0.838              | 0.913             | 0.872               |
| RMFormer (Deng et al., 2023) | 0.049            | 0.775              | 0.892             | 0.862               | 0.030            | 0.850              | 0.928             | 0.907               | 0.028          | 0.917              | 0.957             | 0.933               | 0.024          | 0.908              | 0.960             | 0.930               | 0.057           | 0.827              | 0.909             | 0.869               |
| GPONet (Yi et al., 2024)     | <b>0.045</b>     | 0.788              | 0.889             | <b>0.865</b>        | 0.027            | 0.858              | 0.937             | 0.912               | 0.025          | 0.925              | 0.964             | <b>0.942</b>        | 0.023          | 0.918              | 0.962             | <b>0.936</b>        | 0.055           | 0.836              | 0.908             | 0.870               |
| VST-T++ (Liu et al., 2024a)  | 0.046            | 0.778              | 0.892             | 0.853               | 0.028            | 0.869              | 0.943             | 0.901               | 0.025          | 0.930              | <b>0.968</b>      | 0.937               | 0.024          | 0.919              | <b>0.968</b>      | 0.930               | <b>0.051</b>    | 0.841              | 0.901             | 0.878               |
| RUN (Ours)                   | <b>0.045</b>     | <b>0.793</b>       | <b>0.893</b>      | <b>0.867</b>        | <b>0.022</b>     | <b>0.886</b>       | <b>0.953</b>      | <b>0.916</b>        | <b>0.023</b>   | <b>0.935</b>       | <b>0.971</b>      | <b>0.941</b>        | <b>0.022</b>   | <b>0.927</b>       | <b>0.970</b>      | 0.934               | <b>0.051</b>    | <b>0.843</b>       | <b>0.925</b>      | <b>0.883</b>        |

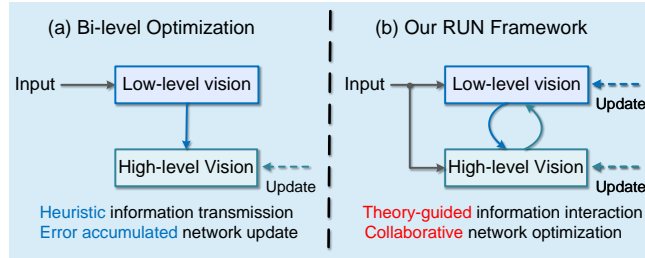


Figure S2. Comparison between bi-level optimization and our RUN.

**Salient object detection.** We evaluate the performance of our method on five widely used benchmark datasets: *DUT-OMRON* (Yang et al., 2013), *DUTS-test* (Wang et al., 2017), *ECSSD* (Yan et al., 2013), *HKU-IS* (Li & Yu, 2015), and *PASCAL-S* (Li et al., 2014). The *DUTS* dataset contains 10,553 training images and 5,019 test images, referred to as *DUTS-test*. The *DUT-OMRON* and *ECSSD* datasets include 5,168 and 1,000 images, respectively. The *HKU-IS* dataset consists of 4,447 images featuring multiple foreground salient objects, while *PASCAL-S* comprises 850 images derived from the *PASCAL VOC 2010* dataset (Everingham et al., 2010). For evaluation, we use the same metrics applied in COD.

## A.2. Generalization on concealed defect detection

We evaluate the generalization capability of our RUN framework in the concealed defect detection task by directly using the model trained on the COD task. Detailed information about the experimental setup can be found in Appendix A.1. As shown in Table S1, our method achieves superior performance compared to existing state-of-the-art approaches, further highlighting the advancements and effectiveness of the RUN framework.

## A.3. Generalization on salient object detection

We evaluate the generalization of our method in salient object detection. Details regarding the training configurations and datasets are provided in Appendix A.1. As shown in Table S2, our method outperforms existing state-of-the-art approaches, achieving a leading position. These results highlight the superiority of our approach and underscore the potential of unfolding-based frameworks for high-level vision tasks.

## B. Limitations and Future Work

As illustrated in Fig. 5, our RUN model, like other advanced methods, exhibits instability in degraded scenarios. This is primarily because environmental degradation exacerbates the challenge of extracting subtle discriminative information, bringing difficulties in capturing concealed objects. However, RUN+ demonstrates robustness to haze degradation, underscoring the potential of the RUN-based framework for addressing scenarios involving environmental degradation.

Future work will focus on integrating the RUN model with more advanced low-level vision algorithms to address increasingly

complex scenarios involving diverse types of degradation, such as low light, blur, and noise. Additionally, incorporating large-scale algorithms into the unfolding-based multi-stage framework introduces significant computational and storage demands. Developing strategies to effectively integrate degradation-resistant models within this framework remains an important research direction.

Furthermore, as this work represents a pioneering effort in applying deep unfolding networks (DUNs) to high-level vision tasks, it opens the door for the development of more DUN-based algorithms in this domain. These future approaches are expected to better balance interpretability and generalizability, further advancing high-level vision tasks. Additionally, establishing an unfolding-based high-resolution COS method (Zheng et al., 2024) is also our goal.